JOURNAL OF THE MECHANICAL BEHAVIOR OF BIOMEDICAL MATERIALS 30 (2014) 234–243

Available online at www.sciencedirect.com

ScienceDirect

www.elsevier.com/locate/jmbbm

A probabilistic damage model based on direct 3-D correlation of strain to damage formation following fatigue loading of rat femora ☆

Joshua A. Gargac[a], *Travis L. Turnbull*[b], *Ryan K. Roeder*[a,b], *Glen L. Niebur*[a,b,*]

[a]*Bioengineering Graduate Program, University of Notre Dame, Notre Dame, IN, USA*
[b]*Department of Aerospace and Mechanical Engineering, University of Notre Dame, Notre Dame, IN, USA*

ARTICLE INFO

Article history:
Received 29 July 2013
Received in revised form
11 November 2013
Accepted 13 November 2013
Available online 25 November 2013

Keywords:
Microdamage
Cortical bone
Finite element modeling
Weibull distribution
Rat femur

ABSTRACT

Microdamage accumulates in bone due to repetitive or excessive mechanical loading, and accumulation of damage can lead to an increase in fracture susceptibility. Understanding the stress or strain criterion for damage formation would allow improved predictive modeling to better assess experimental results or evaluate training regimens. Finite element models coupled with three-dimensional measurements of damage were used to directly correlate damage formation to the local strain state in whole rat femora subjected to three-point bending fatigue. Images of accumulated damage from contrast-enhanced micro-CT were overlaid onto the calculated strain result to determine the strain associated with damage. Most microdamage accumulated in areas where the first principal strain exceeded 0.5%, but damage also occurred at lower strains when applied over sufficiently large volumes. As such, a single threshold strain was not a good predictor of damage. In order to capture the apparently stochastic nature of damage formation, a Weibull statistical model was applied. The model provided a good fit to the data, and a fit based on a subset of the data was able to predict the results in the remaining samples with an RMS error of 17%. These results demonstrate that damage formation is dependent on principal strain, but has a random component that is likely due to the presence of pores or flaws smaller than the resolution of the model that act as stress concentrations in bone.

1. Introduction

Microdamage accumulates in cortical bone due to repetitive or excessive mechanical loading (Norman and Wang, 1997; O'Brien et al., 2003; Schaffler et al., 1989) and with age (Burr et al., 1997; Norman and Wang, 1997; O'Brien et al., 2003; Schaffler et al., 1995; Schaffler et al., 1989). Fatigue damage has been indicated as a stimulus for bone remodeling (Burr et al., 1985). However, harmful levels of accumulated damage can occur when the capacity for bone repair is exceeded by the rate of damage formation, resulting in decreased elastic modulus (Pattin et al., 1996; Schaffler et al., 1989) and fracture toughness (Norman et al., 1998). Ultimately, excessive damage accumulation is manifested as a stress fracture (Lee et al., 2000; O'Brien et al., 2003). The ability to assess the risk of damage accumulation in response to implanted devices, exercise, or training regimens would reduce injuries and improve training or rehabilitation safety.

Damage occurs in highly stressed regions of cortical bone (Fondrk et al., 1999; George and Vashishth, 2005), with most

☆The data for the models in this paper can be downloaded as a zip file from the site <http://bones.ame.nd.edu/GargacEtAlJMBBM?>.

*Corresponding author at: Department of Aerospace and Mechanical Engineering, University of Notre Dame, Notre Dame, IN, USA. Tel.: +1 574 631 3327; fax: +1 574 631 2144.
E-mail address: gniebur@nd.edu (G.L. Niebur).

1751-6161/$ - see front matter © 2013 Elsevier Ltd. All rights reserved.
http://dx.doi.org/10.1016/j.jmbbm.2013.11.009

studies reporting results for controlled loading of machined samples (Diab and Vashishth, 2005; Fondrk et al., 1999; Landrigan et al., 2011; Vashishth et al., 2001). In bending of machined samples, diffuse damage is associated with tensile strain while microcracking is associated with compressive loading (Diab and Vashishth, 2005). However, damage has also been detected in areas of lower strain following bending (Turnbull et al., 2011), suggesting probabilistic characteristics. One hypothesis is that the likelihood of occurrence depends on the both the magnitude of the strain and the size of the volume over which it occurs (Bigley et al., 2007; Taylor, 1998; Taylor and Kuiper, 2001; Taylor et al., 1999). Recent studies have correlated microdamage to calculated strain distributions in 2-D sections of bovine trabecular bone (Nagaraja et al., 2005) and human trabecular bone (Green et al., 2011). Damage was preferentially associated with locations of high strain, but not all highly strained areas were associated with damage. As such, there may be a probabilistic element to damage formation in response to bone strain.

Developing a probabilistic model of damage requires a mapping between locations of damage and the strain distribution during loading. The former can be imaged using contrast-enhanced micro-computed tomography (μCT) after labeling tissue with a barium sulfate ($BaSO_4$) contrast agent (Landrigan et al., 2011; Leng et al., 2008; Turnbull et al., 2011; Wang et al., 2007), and the latter can be calculated using specimen-specific finite element models (Taddei et al., 2006; Torcasio et al., 2012; van Lenthe et al., 2008). The goal of this study was to develop a predictive model for damage formation in fatigue loaded bone. Specifically, (1) locations of damage in whole rat femora subjected to bending fatigue were identified using a contrast agent and 3-D imaging; (2) the strain within the damaged regions was calculated by specimen-specific finite element models; and (3) a predictive criterion for damage formation was developed and assessed.

2. Methods

Twelve fresh-frozen whole femora from mature male Wistar rats were studied. In a previous study (Turnbull et al., 2011), the femora were cyclically fatigued in three-point bending at 2 Hz at a span of 14.5 mm. A specimen-specific peak force was applied to induce a maximum tensile strain of approximately 0.85% on the periosteal surface (Turner and Burr, 1993) until a stiffness degradation of 5% ($N=7$) or 10% ($N=5$) was reached. Following testing, femora were stained with $BaSO_4$ to label damage (Landrigan et al., 2011; Leng et al., 2008; Turnbull et al., 2011; Wang et al., 2007). Briefly, specimens were soaked in a solution of equal parts acetone, phosphate buffered saline (PBS), and 0.5 M $BaCl_2$ (certified ACS crystal, Fisher Scientific Fair Lawn, NJ) in deionized (DI) water for 3 days, followed by a solution of equal parts acetone, PBS and 0.5 M Na_2SO_4 (anhydrous powder, Fisher scientific, Fair Lawn, NJ) in DI water for 3 days, both under vacuum (~50 mm Hg). This method relies on nucleation of $BaSO_4$ crystals within voids in the bone. Specimens were stored at −20 °C in airtight containers containing equal parts PBS and ethanol during interim periods. The 14.5 mm segment of each stained femoral diaphysis, between the two supports from

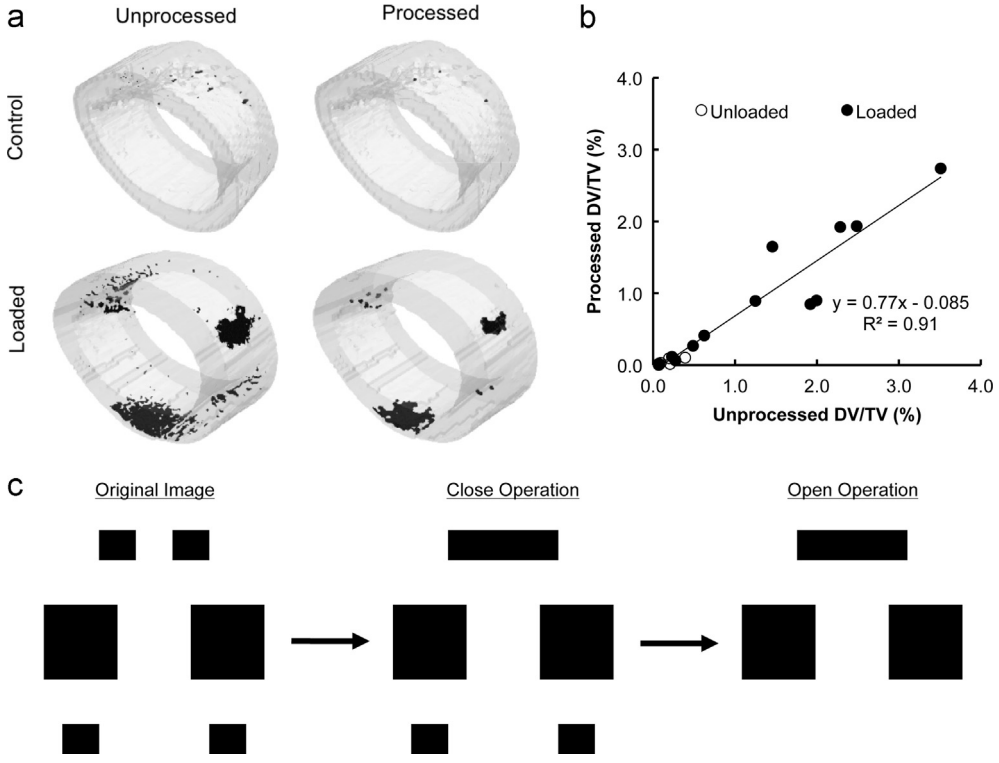

Fig. 1 – In stained control femurs, image processing removed non-specific staining. In loaded femora, the remaining voxels are located in distinct regions. Processing removed approximately 70% of stained voxels in control samples, but only 23% of stained voxels in loaded samples (b). The image processing technique connected small regions of bone labeled by $BaSO_4$ that were in close proximity, but removed small isolated volumes (c).

three-point bending, was imaged in PBS using μCT (μCT-80, Scanco Medical AG, Brüttisellen, Switzerland) at 10 μm resolution, 70 kVp, 114 mA and 400 ms integration time. The images were Gaussian filtered (σ=1.0, support=3.0) and damage was segmented at a constant threshold equivalent to 3310 mg HA/cc, which is higher than bone tissue grayscale (Turnbull et al., 2011).

An image processing technique was developed to separate non-specific $BaSO_4$ staining of porosity from damage. The strategy was to develop an algorithm that removed the majority of stained voxels in images from unloaded femora that should contain minimal damage, while conserving stained regions in loaded samples. Thresholded μCT images of the stained regions were first subjected to a morphological closing by 5 voxels, which connects regions separated by less than ten voxels into single regions. Regions of non-specific staining were subsequently removed by a morphological opening of two voxels, which removes regions with a dimension less than four voxels in any direction. Damaged regions in the processed images were defined as connected volumes of stained voxels. A group of five control samples that had not been loaded were used in addition to the twelve fatigued samples to assess the validity of the method (Fig. 1).

Specimen-specific finite element models of each femur were created to simulate the three-point bending experiment (Fig. 2). Micro-CT images were Gaussian filtered (σ=0.7, support=2.0), downsampled to 80 μm resolution using cubic interpolation, and converted to tetrahedral meshes using a constant threshold of 950 mg HA/cc (Visualization Tool Kit, Kitware, Clifton Park, N.Y.). Laplacian smoothing was applied to the mesh to improve tetrahedral aspect ratios with the surface nodes fixed to maintain the bone volume. The mesh was transferred to a general-purpose finite element program (ADINA 8.7, Watertown, MA). A uniform isotropic Young's modulus was calibrated to match the measured reaction forces specifically for each sample. The mean (± standard deviation) applied modulus was 5.0 (± 2.3) GPa, and Poisson's ratio was assumed to be 0.3. Boundary conditions were applied to simulate the three-point bending supports, and a rigid contact surface mimicking the loading fixture was used to apply a bending load to the same displacement as the initial cycle of fatigue loading (Fig. 2). Nodal strains were found by averaging the calculated element strains. One femur was modeled and solved using 60 μm elements to ensure that the mesh was sufficiently refined.

Processed damage images were overlaid onto the calculated strain field from the models (Fig. 3, Paraview, Kitware, Clifton Park, N.Y.). The strain magnitude located in voxels where damage was present was found for the central 2 mm of each femur. Results from the 5% and 10% stiffness reduction groups were pooled, because there was no statistical difference in the total volume of accumulated damage between the groups in the previous experiment (Turnbull et al., 2011).

A sensitivity study was performed to determine the effect of the selected image threshold on the calculated strain field. One femur was segmented at 5% and 15% higher threshold levels. The same material properties and boundary conditions were

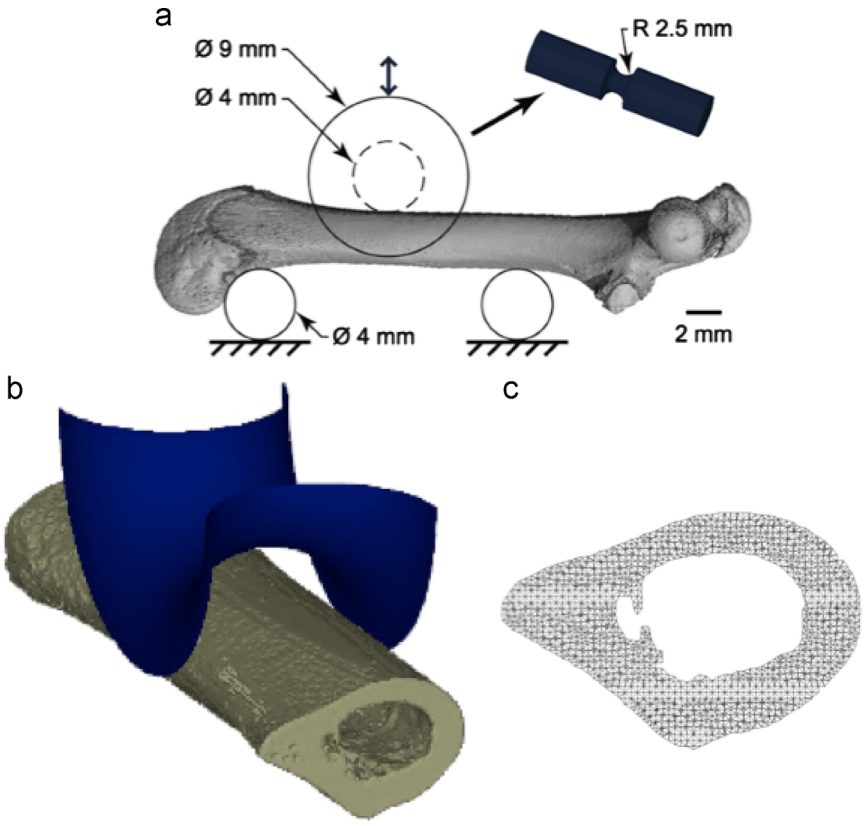

Fig. 2 – (a) Schematic diagram of the three-point bending fixture used to induce damage in rat femurs (Turnbull et al., 2011). (b) The associated finite element model of the upper loading support and a (c) detailed mesh for a femoral cross-section corresponding to the proximal end of the model.

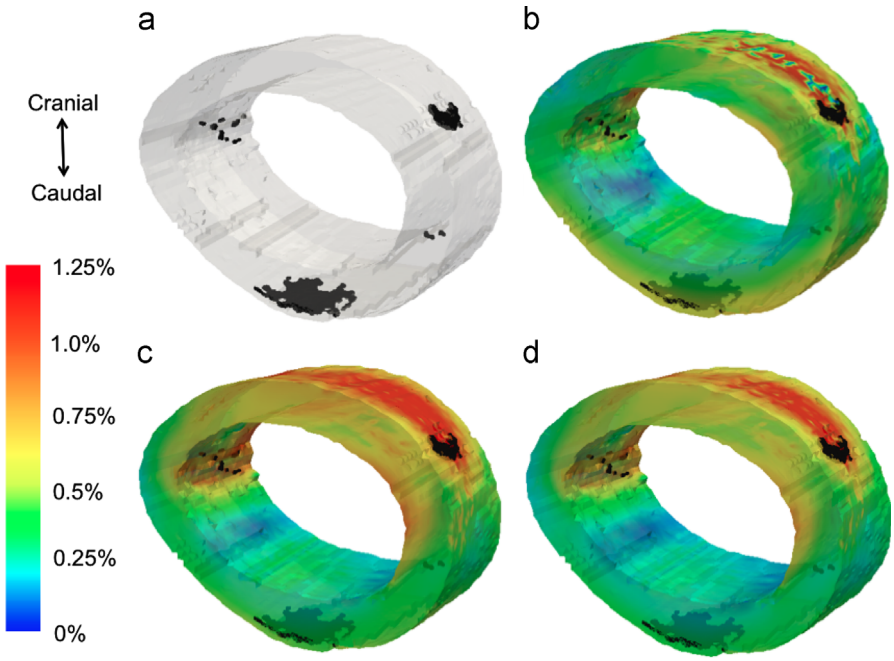

Fig. 3 – 3-D μCT images of stained damage overlaid onto the finite element results. Microdamage (a) coincided with high first principal strains (b), maximum shear strains (c), and octahedral shear (d) strains calculated by the models at the points of load application on the cranial surface and along the tensile caudal surface of the bone.

applied, and the relationship between strain and damage was compared to the original model.

The Weibull distribution (Weibull, 1951) has been proposed to describe the probability of failure in damaging materials (Taylor, 1998; Taylor and Kuiper, 2001; Taylor et al., 1999). According to the theory, most failed volumes should be concentrated in a narrow high strain range, while some failed volumes are dispersed across lower strains. A Weibull parameter plot was used to determine whether the presence of damage followed a Weibull distribution. The bone was discretized into nearly equally sized tetrahedral volumes with approximately 240 μm edges and a mean (± standard deviation) volume of 1.56×10^{-3} ($\pm 0.194 \times 10^{-3}$) mm^3. The tetrahedra containing damage were rank ordered (j_1, j_2, …, j_n) according to the average strain within them to determine the Weibull parameter:

$$y_i = \log_{10}\left[\log_{10}\left(\frac{j_n + 1}{j_n - j_i + 1}\right)\right] \quad (1)$$

Linear regression of the Weibull parameter versus $\log_{10}$(strain) was used to find the Weibull modulus (Bigley et al., 2007; Cattell and Kibble, 2001; Wisnom, 1999).

A model based on the Weibull distribution was used to relate the probability of damage occurring within a region of bone based on the level of strain and the volume of the region. The first principal strain, maximum shear strain, and octahedral shear strain were considered as potential damage criteria. Elements were separated into nine strain ranges: less than 0.2%, 0.2–0.3%, 0.3–0.4%, 0.4–0.5%, 0.5–0.6%, 0.6–0.7%, 0.7–0.8%, 0.8–1.0%, and greater than 1.0% strain. Connected regions of elements for each strain range were found and sorted into five to seven groups of similar sized volumes. A connected region of elements was considered damaged if it contained any $BaSO_4$ labeled voxels. The probability of damage occurring in a region of a given volume and strain level was calculated as the percentage of all such regions across all femora containing damage. The probability was fit to a Weibull distribution based on a strained volumes method:

$$P = 1 - \exp\left[-\frac{V_s}{V_{so}}\left(\frac{\varepsilon}{\varepsilon^*}\right)^m\right] \quad (2)$$

where P represents the probability of damage for a volume, V_s, subjected to a strain, ε (Taylor, 1998; Taylor and Kuiper, 2001; Taylor et al., 1999). In Eq. (2), the Weibull modulus, m, is a constant representing the degree of scatter in the data. Large values of m indicate that microdamage is primarily a factor of the applied strain, while smaller values indicate a greater chance of damage occurring at lower strains. For a volume V_{so} of material subjected to a strain of ε^*, the probability of damage occurring is 0.63 (Taylor and Kuiper, 2001). The constants were optimized using the constrained minimization function, fmincon, in Matlab™ (MathWorks, Natick, MA) to minimize the root-mean-square difference between the measured and predicted probabilities. The initial values for the Weibull modulus, m, were taken from the fit of the Weibull parameter. Several different initial values for the remaining constants were used to ensure the solution was unique.

3. Results

The close and open sequence removed 70% of stained voxels from images of unloaded samples, but removed less than 25% from images of loaded femora (Fig. 1). As a result, only 0.01%

Table 1 – The Weibull model constants found by minimizing the root-mean-squared error between the percentage of damaged volumes at specified strain ranges and volumes and predicted damage probability.

Strain type	Weibull Modulus (m)	Reference Volume (mm^3)	Reference strain
First principal strain	0.8	7.79	0.41
Max shear strain	1.21	8.23	0.49
Octahedral shear strain	1.56	8.05	0.45

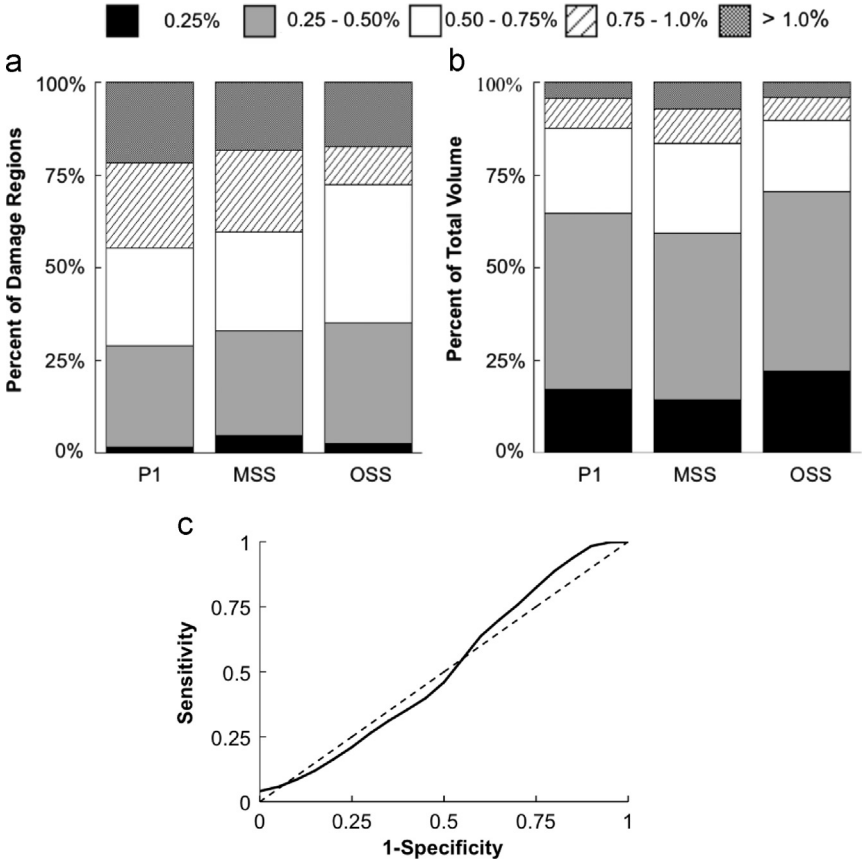

Fig. 4 – The fraction of damaged areas (a) and total volume (b) where the peak strain fell within each strain range of 1st principal strain (P1), maximum shear strain (MSS), and octahedral shear strain (OSS). The receiver operator characteristic curve for varying 1st principal strain indicated that no threshold strain was a suitable predictor of damage (c). Data are pooled for 12 femurs.

of the voxels in the control samples were labeled compared to 1.04% in fatigued samples, on average. Damage density in the processed images was correlated to that measured from the unprocessed images (Fig. 1b), which has been shown to correlate to traditional histologic measures of damage (Landrigan et al., 2011).

Damage was detected in areas of high strain magnitude on the caudal surface of the bones, which was loaded in tension, as well as at the contact point with the loading fixture (Fig. 3). However, a simple strain criterion was neither sensitive nor specific for damage (Fig. 4). Only 70% of damaged regions had principal strains over 0.5%. Similarly, the peak shear and octahedral shear strains exceeded 0.5% in only 65% of the damaged regions. Conversely, while approximately 30% of the total model volume was subjected to strains greater than 0.5% in each mode, only 1.7% of the volume was stained by $BaSO_4$.

The Weibull parameter was linearly correlated to $\log_{10}$(strain) except at the extreme low and high strain values (Fig. 5). The Weibull modulus was equal to 2.5 using first principal strain, 2.8 using octahedral shear strain, and 2.7 based on the maximum shear strain, indicating that damage was detected over a wide strain range.

The probability of damage increased with both the volume of a strained region and its strain magnitude, consistent with a Weibull probability model (Fig. 6). Optimization of the Weibull constants consistently converged to a Weibull modulus of 0.8 when using first principal strain as the criterion, 1.56 when using octahedral shear strain, and 1.21 when using maximum shear strain. The reference strain and volume coefficients converged to different values depending on initial values. Since m was near unity, the fitted values of V_{so} and ε^* were more sensitive to the initial values (Table 1). The

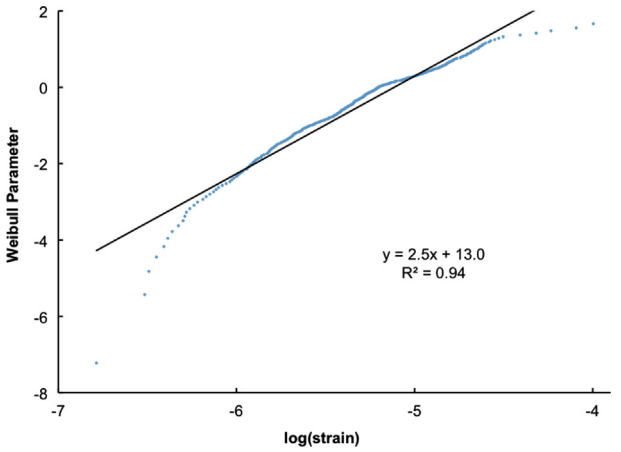

Fig. 5 – The Weibull parameter was plotted as a function of log(strain) to determine whether the data follow a Weibull distribution, and to determine the initial estimate for the Weibull modulus (*m*) to be used in the nonlinear fit. Elements containing damage followed a Weibull distribution with the exception of the extreme low and highly strained elements. Data consisted of 2920 volumes for the 12 femurs.

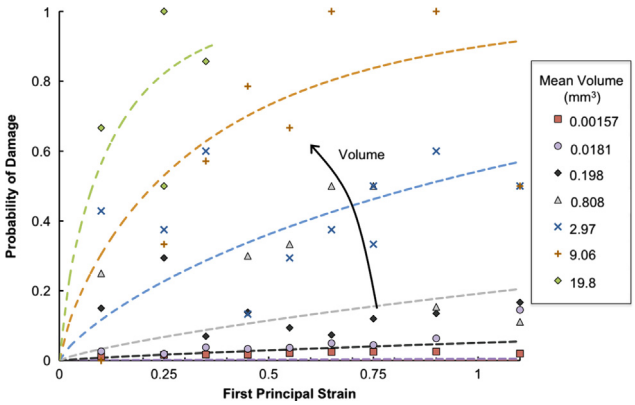

Fig. 6 – The percentage of volumes damaged as a function of first principal strain for different mean volumes. Dashed lines show the Weibull fit from Eq. (1). The probability of damage increased as both volume and strain increased, and displayed the same trend as a Weibull prediction of damage probability. Data was pooled for 12 femora.

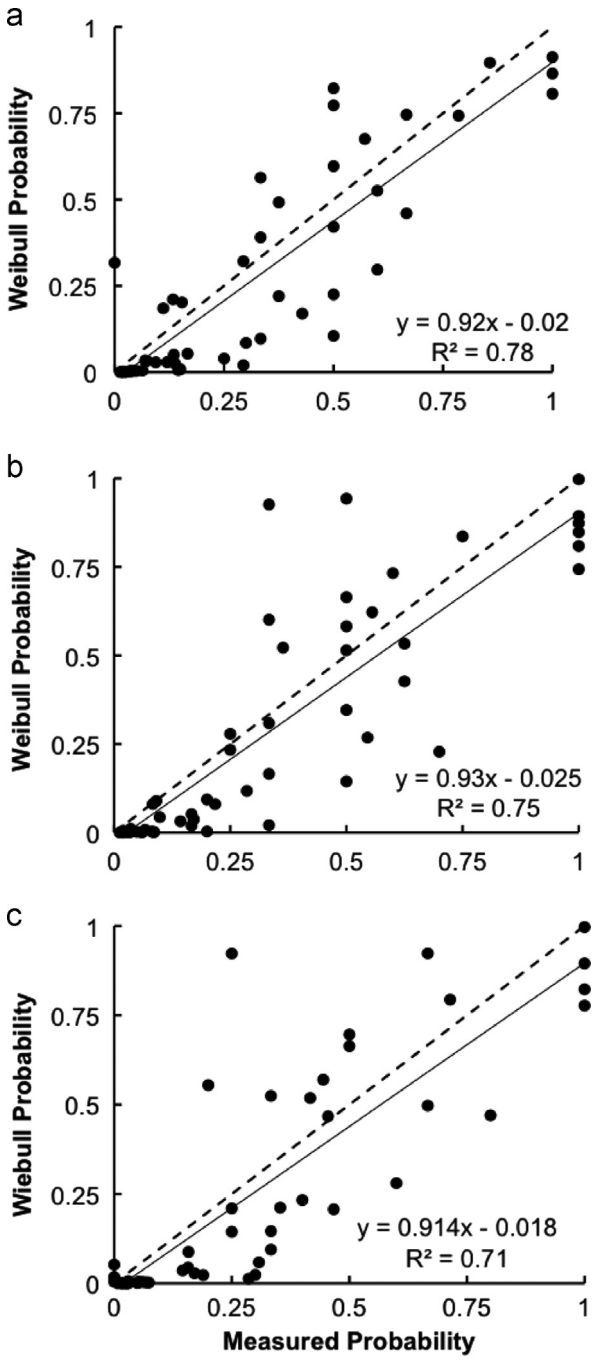

Fig. 7 – The Weibull probability function predicted damage in strained volumes for (a) first principal strain, (b) maximum shear strain, and (c) octahedral shear strain. The probability of damage increased as a function of both strain and volume. Dashed lines show the ideal 1:1 relationship, whereas solid lines show the linear fit for the data. First principal strain provided the best correlation between the actual and predicted damage probability.

Weibull probability was strongly correlated with the observed probability for all three measures of strain (Fig. 7).

The Weibull predictions calibrated using 10 random samples predicted the damage probability in the remaining two samples with an RMS error of 17%. Across all twelve samples, the actual probability of damage agreed well with the Weibull probability based on the fitted parameters (Fig. 8).

Strain magnitudes in damaged regions across the median 2 mm of the femur were minimally sensitive to model resolution or segmentation threshold. The total work done calculated for both 80 μm and 60 μm elements differed by only 7% between the two resolutions. On average, decreasing the element size by 25% only decreased the maximum principal strains in damaged regions by 2.7%. Furthermore, the strain magnitudes were not sensitive to small changes to the selected threshold. On average, increasing the segmentation threshold by 5% decreased the maximum principal strains in damaged regions by 2.6%, which did not change the grouping of damage regions used for constructing the probabilistic model. The simulated stiffness decreased by 2.7%. However, increasing the segmentation threshold by 15% decreased the maximum principal strains

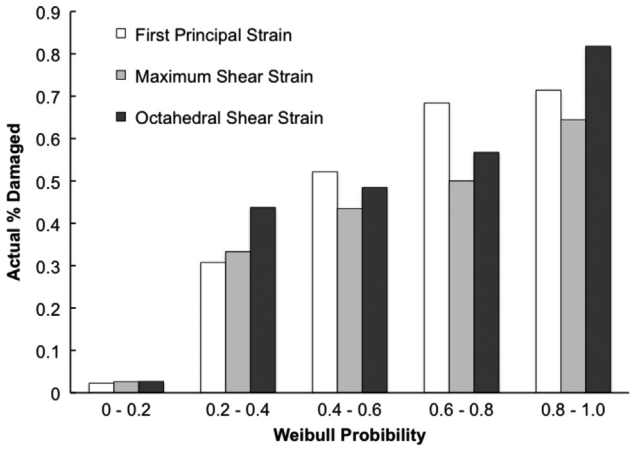

Fig. 8 – The probability of damage was calculated for each connected volume of tissue based on the fitted Weibull parameters. The fraction of regions that were damaged within each probability range agreed well with the calculated probability of damage. Data used is the pooled total of damaged volumes across 12 femora.

in damaged regions by as much 9.23%, which did affect the assignment of damaged regions to associated strained volumes.

4. Discussion

This study employed finite element modeling and a novel 3-D damage imaging technique to study criteria for damage formation in rat bones loaded in three-point bending fatigue. Regions of high strain exhibited a high probability of containing damage, but not all damage was found at high strains. As such, a single criterion was not capable of identifying damaged sites, and a probabilistic model was pursued. The Weibull distribution provided a good prediction of the probability of damage occurrence in regions subjected to low strain observed in the experiment. The Weibull modulus was near 1.0, suggesting damage is somewhat stochastic in bone (Huiskes et al., 2000). Finally, the results of this methodology indicate that for a volume of bone experiencing a given strain, the majority of the volume is not damaged.

A strained volume model was used to relate the probability of microdamage to the calculated strain distribution from the first loading cycle. Such a model is applicable in materials that contain flaws or pores that act as stress concentrations (Bigley et al., 2007; Taylor and Kuiper, 2001). In addition, this study applied a novel method of implementing the Weibull model to a three-point bending test wherein a range of strains occurs within the same sample. Finally, 3-D quantification and correlation using contrast-enhanced μCT enabled the visualization and analysis of damage throughout the sample, and direct comparison to the calculated strains .

There are some important limitations to consider in this study. First, microdamage was created by fatigue loading (Turnbull et al., 2011), while the finite element models only simulated the initial load cycle. However, regions where the highest strain occurs initially are likely locations for damage initiation (Kotha et al., 2004), and continued fatigue loading would be expected to propagate this damage. Second, $BaSO_4$ staining is not specific to microdamage. As such, some stained regions may represent intracortical or endosteal porosity rather than damage (Turnbull et al., 2011). However, the morphological image processing was demonstrated to remove most non-specific staining from samples that had not been loaded and presumably contained minimal damage, while leaving the majority of stained voxels in loaded specimens. Furthermore, when applied to images of fatigued samples, the number of voxels removed increased 16 fold compared to control samples. As such, the image processing technique may have removed areas of real damage with dimensions less than 40 μm in any dimension. Finally, generation of a finite element mesh from μCT images is inherently dependent on the image processing parameters, filtering, and selected threshold (Davis et al., 2007; Palacio-Mancheno et al., 2013). A sensitivity analysis on one femur showed that the probabilistic model was not sensitive to small variations in the segmentation parameters used to create the finite element mesh.

The Weibull model provides a probability of damage occurring rather than an absolute criterion. In this analysis, the Weibull modulus of $m \approx 1$ was lower than the reported value of 8 for fatigue failure of human compact bone (Taylor, 1998). This suggests that while strain is a very good predictor of overall failure in bone, microdamage induced by three-point bending is more heterogeneous in nature, and damage is likely to be found within any sufficiently large volume subjected to a load. This is consistent with a large quantity of pores, such as osteocyte lacunae that act as stress concentrations and increase the susceptibility to damage formation, and with the existence of spatially random diffuse microdamage in bone of normally functioning individuals (Vashishth et al., 2000). Random damage processes have also been used as the basis of bone remodeling algorithms with good success (Huiskes et al., 2000). The low Weibull modulus from this analysis further suggests the presence of damage does not necessarily imply failure, and that much of the damage may not be important to bone failure or remodeling. This agrees well with recent data indicating the inability of diffuse microdamage to initiate a remodeling response (Herman et al., 2010).

The threshold for damage was approximately 0.5% strain, regardless of the strain measure employed. This is similar to reports for human femoral and bovine tibial trabecular bone, where damage occurred between 0.35 and 0.7% octahedral shear strain, or 0.6 and 1.0% first principal strain (Green et al., 2011; Nagaraja et al., 2005). The strain levels are consistent with bovine cortical bone, where elevated 1st principal strains of 1.06% corresponded to $BaSO_4$ staining for machine notched specimens (Leng et al., 2008). Similarly, the strain was about 1.0% near osteocyte lacunae associated with microcracking (Nicolella et al., 2001).

In this study, several assumptions were made to simplify the finite element analysis. First, homogenous material properties were assigned to the models. Non-homogenous material properties can be assigned based on X-ray attenuation (Austman et al., 2008; Bourne and van der Meulen, 2004; Jaasma et al., 2002; van Ruijven et al., 2007), and would affect the calculated strain magnitudes. The inclusion of mineral heterogeneity has been shown to improve the accuracy of computational models (Christen et al., 2013; Donnelly et al., 2010; Kim et al., 2012). Recently, it was shown that non-linear

FE models of damage in the human radius created from high resolution quantitative computed tomography contain information independent from linear simulations (Christen et al., 2013). Furthermore, nearly 97% of variability of humeral strength can be explained by moment of inertia, total mineral density, and mineral:matrix ratio (Donnelly et al., 2010). However, when applied to models of human trabecular bone, strains levels differed by less than 4% of the original predictions (Green et al., 2011). The reported homogeneous elastic modulus ranges orders of magnitude from over 130 MPa (Beaupied et al., 2006) to 1000 MPa (Nazarian et al., 2011). The elastic modulus values used in this study were determined by matching the force-displacement curves from the finite element model to the curves from the *ex vivo* femur loading and were the similar to previously reported values for rat femurs (Jorgensen et al., 1991).

Microstructural bone features including osteocyte lacunae, pores and resorption cavities where not integrated into the model. The inclusion of these features in a high-resolution or multiscale model might provide an explanation for damage in regions subjected to low strain (Voide et al., 2011). For instance, mechanical failure in human vertebral cancellous bone has been shown to preferentially begin near resorption cavities (Slyfield et al., 2012). However, the purpose of a statistical model is to account for such microstructural flaws without resorting to detailed modeling. As such, the low Weibull modulus associated with damage may reflect the fact that flaws such as osteocyte lacunae, canaliculi, and other pores are present at high density throughout the bone. The model could theoretically be calibrated to account for differing densities of microstructural defects either between or within bones.

This study focused on the portion of the bone surrounding the central loading point. Focusing on this region allowed for a comparison of the largest range of strain variation to the highest occurrence of microdamage (Turnbull et al., 2011). To verify that the method was suitable over larger regions, the Weibull analysis was repeated on 4 samples across the central 6 mm. Similar trends were observed, with damage at a given strain being more probable when it was applied over a larger region. The optimized prediction obtained using the 2 mm region was applied to the larger 6 mm region and the RMS error increased from 28% to 35%. The greater proportion of low strain regions and the absence of highly strained regions outside the central 2 mm taken together affected the quality of the fit.

Uncertainties in the model parameters can propagate to affect the results. There is some uncertainty in our modulus calculations, because we did not include changes in modulus due to damage accumulation during loading. However, a material model governing both creep and damage formation in rat bone has not been established, and as such we chose to consider the initial elastic behavior with the assumption that damage initiated early and propagated during the fatigue process. The segmentation threshold, which changes the bone geometry, can also be a source of error in image based finite element models. We verified that the data are relatively insensitive to these uncertainties by parametrically varying the threshold over a reasonable range. Finally, identification of damage in image-based methods also has inherent uncertainty. These effects were limited by identifying large contiguous stained regions, and then determining the strain within them. Hence, slight changes in the location or volume of the stained regions had minimal affect on the results. Smaller stained regions were deleted if they were distant from other regions, or grouped into larger regions. As such, the effects of noise in the image and staining of small pores were mitigated. Moreover, 3-D quantification of damage can eliminate uncertainty associated with sampling that is inherent to histological methods (Bigley et al., 2008; Martin et al., 2007).

The damage criteria considered were isotropic, and did not account for strain orientation relative to the microstructure. Accounting for the strain orientation would likely have an effect, as cracks tend to grow along lamellae and arrest while crossing lamellae. In some regions, damage was associated with high shear strain with low tensile principal strain, suggesting a potential role for shear or compressive strain in this experiment. The significance of shear forces in damage formation has not been well documented. The highest shear strain is oriented off axis to the bone and material axes at the location of maximum tension or compression during bending of whole bone. In contrast, near the neutral axis there is a high shear stress oriented along the length of the bone that could cause defects between microstructural features. However little damage was detected at the neutral axis. As such, neither maximum shear strain nor octahedral shear strain improved the predictive power of the Weibull distribution when compared to the first principal strain. Taken together, this result suggested a minimal effect from shear strains in the experiment.

The predictive power of a Weibull statistical model accounts for microdamage accumulation at low strains. This model could be integrated into Monte Carlo simulations to model damage accumulation for bone adaptation or stress fracture predictions (Pidaparti et al., 2001).

Acknowledgments

This study was supported by the U.S. Army Telemedicine and Advanced Technology Research Center W81XWH-09-1-0741.

REFERENCES

Austman, R.L., Milner, J.S., Holdsworth, D.W., Dunning, C.E., 2008. The effect of the density-modulus relationship selected to apply material properties in a finite element model of long bone. J. Biomech. 41, 3171–3176.

Beaupied, H., Dupuis, A., Arlettaz, A., Brunet-Imbault, B., Bonnet, N., Jaffre, C., Benhamou, C.L., Courteix, D., 2006. The mode of bone conservation does not affect the architecture and the tensile properties of rat femurs. Biomed. Mater. Eng. 16, 253–259.

Bigley, R.F., Gibeling, J.C., Stover, S.M., Hazelwood, S.J., Fyhrie, D.P., Martin, R.B., 2007. Volume effects on fatigue life of equine cortical bone. J. Biomech. 40, 3548–3554.

Bigley, R.F., Singh, M., Hernandez, C.J., Kazakia, G.J., Martin, R.B., Keaveny, T.M., 2008. Validity of serial milling-based imaging system for microdamage quantification. Bone 42, 212–215.

Bourne, B.C., van der Meulen, M.C., 2004. Finite element models predict cancellous apparent modulus when tissue modulus is scaled from specimen CT-attenuation. J. Biomech. 37, 613–621.
Burr, D.B., Forwood, M.R., Fyhrie, D.P., Martin, R.B., Schaffler, M.B., Turner, C.H., 1997. Bone microdamage and skeletal fragility in osteoporotic and stress fractures. J. Bone Mineral Res. 12, 6–15.
Burr, D.B., Martin, R.B., Schaffler, M.B., Radin, E.L., 1985. Bone remodeling in response to in vivo fatigue microdamage. J. Biomech. 18, 189–200.
Cattell, M.K., Kibble, K.A., 2001. Determination of the relationship between strength and test method for glass fibre epoxy composite coupons using Weibull analysis. Mater. Des. 22, 245–250.
Christen, D., Zwahlen, A., Muller, R., 2014. Reproducibility for linear and nonlinear micro-finite element simulations with density derived material properties of the human radius. J. Mech. Behav. Biomed. Mater. 29, 500–507.
Davis, K.A., Burghardt, A.J., Link, T.M., Majumdar, S., 2007. The effects of geometric and threshold definitions on cortical bone metrics assessed by in vivo high-resolution peripheral quantitative computed tomography. Calcif. Tissue Int. 81, 364–371.
Diab, T., Vashishth, D., 2005. Effects of damage morphology on cortical bone fragility. Bone 37, 96–102.
Donnelly, E., Chen, D.X., Boskey, A.L., Baker, S.P., van der Meulen, M.C., 2010. Contribution of mineral to bone structural behavior and tissue mechanical properties. Calcif. Tissue Int. 87, 450–460.
Fondrk, M.T., Bahniuk, E.H., Davy, D.T., 1999. A damage model for nonlinear tensile behavior of cortical bone. J. Biomech. Eng.-Trans. ASME 121, 533–541.
George, W.T., Vashishth, D., 2005. Damage mechanisms and failure modes of cortical bone under components of physiological loading. J. Orthop. Res. 23, 1047–1053.
Green, J.O., Nagaraja, S., Diab, T., Vidakovic, B., Guldberg, R.E., 2011. Age-related changes in human trabecular bone: relationship between microstructural stress and strain and damage morphology. J. Biomech. 44, 2279–2285.
Herman, B.C., Cardoso, L., Majeska, R.J., Jepsen, K.J., Schaffler, M. B., 2010. Activation of bone remodeling after fatigue: differential response to linear microcracks and diffuse damage. Bone 47, 766–772.
Huiskes, R., Ruimerman, R., van Lenthe, G.H., Janssen, J.D., 2000. Effects of mechanical forces on maintenance and adaptation of form in trabecular bone. Nature 405, 704–706.
Jaasma, M.J., Bayraktar, H.H., Niebur, G.L., Keaveny, T.M., 2002. Biomechanical effects of intraspecimen variations in tissue modulus for trabecular bone. J. Biomech. 35, 237–246.
Jorgensen, P.H., Bak, B., Andreassen, T.T., 1991. Mechanical properties and biochemical composition of rat cortical femur and tibia after long-term treatment with biosynthetic human growth hormone. Bone 12, 353–359.
Kim, G., Boskey, A.L., Baker, S.P., van der Meulen, M.C., 2012. Improved prediction of rat cortical bone mechanical behavior using composite beam theory to integrate tissue level properties. J. Biomech. 45, 2784–2790.
Kotha, S.P., Hsieh, Y.F., Strigel, R.M., Muller, R., Silva, M.J., 2004. Experimental and finite element analysis of the rat ulnar loading model – correlations between strain and bone formation following fatigue loading. J. Biomech. 37, 541–548.
Landrigan, M.D., Li, J., Turnbull, T.L., Burr, D.B., Niebur, G.L., Roeder, R.K., 2011. Contrast-enhanced micro-computed tomography of fatigue microdamage accumulation in human cortical bone. Bone 48, 443–450.
Lee, T.C., O'Brien, F.J., Taylor, D., 2000. The nature of fatigue damage in bone. Int. J. Fat. 22, 847–853.
Leng, H.J., Wang, X., Ross, R.D., Niebur, G.L., Roeder, R.K., 2008. Micro-computed tomography of fatigue microdamage in cortical bone using a barium sulfate contrast agent. J. Mech. Behav. Biomed. Mater. 1, 68–75.
Martin, R.B., Yeh, O.C., Fyhrie, D.P., 2007. On sampling bones for microcracks. Bone 40, 1159–1165.
Nagaraja, S., Couse, T.L., Guldberg, R.E., 2005. Trabecular bone microdamage and microstructural stresses under uniaxial compression. J. Biomech. 38, 707–716.
Nazarian, A., Araiza Arroyo, F.J., Rosso, C., Aran, S., Snyder, B.D., 2011. Tensile properties of rat femoral bone as functions of bone volume fraction, apparent density and volumetric bone mineral density. J. Biomech. 44, 2482–2488.
Nicolella, D.P., Nicholls, A.E., Lankford, J., Davy, D.T., 2001. Machine vision photogrammetry: a technique for measurement of microstructural strain in cortical bone. J. Biomech. 34, 135–139.
Norman, T.L., Wang, Z., 1997. Microdamage of human cortical bone: incidence and morphology in long bones. Bone 20, 375–379.
Norman, T.L., Yeni, Y.N., Brown, C.U., Wang, Z., 1998. Influence of microdamage on fracture toughness of the human femur and tibia. Bone 23, 303–306.
O'Brien, F.J., Taylor, D., Lee, T.C., 2003. Microcrack accumulation at different intervals during fatigue testing of compact bone. J. Biomech. 36, 973–980.
Palacio-Mancheno, P.E., Larriera, A.I., Doty, S.B., Cardoso, L., Fritton, S.P., 2013. 3D assessment of cortical bone porosity and tissue mineral density using high-resolution micro-CT: effects of resolution and threshold method. J. Bone Miner. Res..
Pattin, C.A., Caler, W.E., Carter, D.R., 1996. Cyclic mechanical property degradation during fatigue loading of cortical bone. J. Biomech. 29, 69–79.
Pidaparti, R.M., Wang, Q.Y., Burr, D.B., 2001. Modeling fatigue damage evolution in bone. Bio-Med. Mater. Eng. 11, 69–78.
Schaffler, M.B., Choi, K., Milgrom, C., 1995. Aging and matrix microdamage accumulation in human compact bone. Bone 17, 521–525.
Schaffler, M.B., Radin, E.L., Burr, D.B., 1989. Mechanical and morphological effects of strain rate on fatigue of compact-bone. Bone 10, 207–214.
Slyfield, C.R., Tkachenko, E.V., Fischer, S.E., Ehlert, K.M., Yi, I.H., Jekir, M.G., O'Brien, R.G., Keaveny, T.M., Hernandez, C.J., 2012. Mechanical failure begins preferentially near resorption cavities in human vertebral cancellous bone under compression. Bone 50, 1281–1287.
Taddei, F., Cristofolini, L., Martelli, S., Gill, H.S., Viceconti, M., 2006. Subject-specific finite element models of long bones: an in vitro evaluation of the overall accuracy. J. Biomech. 39, 2457–2467.
Taylor, D., 1998. Fatigue of bone and bones: an analysis based on stressed volume. J. Orthop. Res. 16, 163–169.
Taylor, D., Kuiper, J.H., 2001. The prediction of stress fractures using a 'stressed volume' concept. J. Orthop. Res. 19, 919–926.
Taylor, D., O'Brien, F., Prina-Mello, A., Ryan, C., O'Reilly, P., Lee, T.C., 1999. Compression data on bovine bone confirms that a "stressed volume" principle explains the variability of fatigue strength results. J. Biomech. 32, 1199–1203.
Torcasio, A., Zhang, X.L., Duyck, J., van Lenthe, G.H., 2012. 3D characterization of bone strains in the rat tibia loading model. Biomech. Model. Mechanobiology 11, 403–410.
Turnbull, T.L., Gargac, J.A., Niebur, G.L., Roeder, R.K., 2011. Detection of fatigue microdamage in whole rat femora using contrast-enhanced micro-computed tomography. J. Biomech. 44, 2395–2400.
Turner, C.H., Burr, D.B., 1993. Basic biomechanical measurements of bone – a tutorial. Bone 14, 595–608.
van Lenthe, G.H., Voide, R., Boyd, S.K., Muller, R., 2008. Tissue modulus calculated from beam theory is biased by bone size and geometry: implications for the use of three-point

bending tests to determine bone tissue modulus. Bone 43, 717–723.
van Ruijven, L.J., Mulder, L., van Eijden, T.M.G.J., 2007. Variations in mineralization affect the stress and strain distributions in cortical and trabecular bone. J. Biomech. 40, 1211–1218.
Vashishth, D., Koontz, J., Qiu, S.J., Lundin-Cannon, D., Yeni, Y.N., Schaffler, M.B., Fyhrie, D.P., 2000. In vivo diffuse damage in human vertebral trabecular bone. Bone 26, 147–152.
Vashishth, D., Tanner, K.E., Bonfield, W., 2001. Fatigue of cortical bone under combined axial-torsional loading. J. Orthop. Res. 19, 414–420.
Voide, R., Schneider, P., Stauber, M., van Lenthe, G.H., Stampanoni, M., Muller, R., 2011. The importance of murine cortical bone microstructure for microcrack initiation and propagation. Bone 49, 1186–1193.
Wang, X., Masse, D.B., Leng, H., Hess, K.P., Ross, R.D., Roeder, R.K., Niebur, G.L., 2007. Detection of trabecular bone micro-damage by micro-computed tomography. J. Biomech. 40, 3397–3403.
Weibull, W., 1951. A statistical distribution function of wide applicability. J. Appl. Mech.–Trans. ASME 18, 293–297.
Wisnom, M.R., 1999. Size effects in the testing of fibre-composite materials. Compos. Sci. Technol. 59, 1937–1957.